IRS-Enabled Beam-Space Channel

Musab Alayasra, *Student Member, IEEE*, and Hüseyin Arslan, *Fellow, IEEE*

***Abstract*— The intelligent reflecting surface (IRS) is emphasized as a controlled scattering cluster. To this end, scatterers and traveling paths of multipath components are classified to build a new channel model. Unlike the conventional modeling, where the channels between system units are modeled independently, the new model considers the channel as a whole and decomposes it based on the traveling paths. The model shows clearly how IRS, in the beam-space context, converts the channel from a problem into a design element. After investigating IRS as a scattering cluster, based on a proposed segmentation scheme, the beamforming problem is considered with a focus on first-order reflections. Passive beamforming at IRS is shown to have two tiers; at the scatterer and antenna levels. A segment-activation scheme is proposed to maximize the received signal power, where the number of transmitting antenna elements to be used is given as a function of IRS positioning and beamforming at the receiver. The results show that while using more transmitting antenna elements to get narrower beams is possible, using fewer elements can give better performance, especially for larger IRS at close distances. The developed model also proves useful in addressing emerging issues in massive MIMO communication, namely, stationarity and spherical wavefronts.**

***Index Terms*— Beam-space channel, geometric channel, intelligent reflecting surface (IRS), mmWave communication.**

I. Introduction

With every new wireless communication generation, the demand for more resources and better services by emerging applications is accelerating. In response to their urging calls, new generations also come with novel solutions. One example is mmWave technology that proved to be a key player in enhancing spectral efficiency and accommodating demanding applications. Another prominent example is the recently proposed concept called intelligent reflecting surface (IRS) [1]–[3]. As a controlled reflecting object, IRS can be thought of as a *controlled scattering cluster* in the environment responsible for a group of multipath components (MPCs) reflected toward a receiver, which enables a degree of control over the wireless channel. This paradigm shift in wireless communication systems could open the door for promising solutions that were never possible before.

Many works on this topic have been recently reported to improve different aspects of the wireless communication system like information and secrecy rates [4]–[7], power efficiency [8]–[10], multiple accessing [11]–[13], and others [14], [15]. However, the channel model adopted by almost all works shows a common perspective that treats IRS as a third communication unit along with transmitter and receiver without demonstrating clearly its role as a controlled object in the environment. As such, the fundamental antenna-domain channel model is adopted in describing the IRS-enabled wireless channel as a cascade of two channels in addition to the main one, which is given as $\mathbf{G\Phi F}+\mathbf{H}_{\mathrm{D}}$, where $\mathbf{H}_{\mathrm{D}}$ is the channel between transmitter and receiver, $\mathbf{F}$ and $\mathbf{G}$ are, respectively, the channels between IRS and each of transmitter and receiver, and $\mathbf{\Phi}$ is a diagonal matrix representing phase shifts introduced by IRS elements. Besides, the estimation of these channels has an overhead issue due to the large number of antenna elements at IRS [16]–[18], and possibly at the transmitting and receiving units. The sparsity of mmWave channel can be exploited to reduce this overhead [19], [20]. However, as IRS is envisioned to have large sizes covering walls and objects in the environment [3], the assumption of far-field operation is not practical and there could be a non-stationarity [21] over the IRS surface, where different segments of its elements experience different sets of scattering clusters with transmitter or receiver.

Millimeter waves have some features that make a difference in the context of IRS. Their relatively shorter wavelengths result in higher path loss but at the same time allow packing more antenna elements into a compact size to generate narrower beams with higher beamforming gain [22]. Directed beams and high path loss render mmWave channels sparser in general with less number of MPCs and lower-order reflections [21], [23]. For instance, at the 60GHz band in indoor environments, the campaigns in [24] show that the number of scattering clusters ranges from 2 to 5 clusters. At the same band, it is shown in [25] that the power ratio of first to second-order reflection is similar to that of LoS path to first-order reflection with an approximate value of 13dB. In addition to their definite advantage in terms of received power, focusing on first-order reflections in proposing IRS-based solutions (i.e., reflections by IRS only) reduces the overhead of channel estimation mentioned above. Since only LoS links with IRS are utilized, small-scale fading information in $\mathbf{F}$ and $\mathbf{G}$ can be safely ignored. This fact is better understood and exploited if the channel is described geometrically.

At mmWave frequencies, thinking of the channel geometrically is essential to reduce implementation complexity [26].

Manuscript received January 17, 2021; revised May 24, 2021 and August 16, 2021; accepted October 24, 2021. Date of publication November 15, 2021; date of current version June 10, 2022. The work of Hüseyin Arslan was supported by the Scientific and Technological Research Council of Turkey (TUBITAK) under Grant 120C142. The associate editor coordinating the review of this article and approving it for publication was C.-K. Wen. *(Corresponding author: Musab Alayasra.)*

Musab Alayasra is with the Department of Electrical and Electronics Engineering, Istanbul Medipol University, 34810 Istanbul, Turkey (e-mail: musab.alayasra@std.medipol.edu.tr).

Hüseyin Arslan is with the Department of Electrical and Electronics Engineering, Istanbul Medipol University, 34810 Istanbul, Turkey, and also with the Department of Electrical Engineering, University of South Florida, Tampa, FL 33620 USA (e-mail: arslan@usf.edu).

Color versions of one or more figures in this article are available at https://doi.org/10.1109/TWC.2021.3124288.

Digital Object Identifier 10.1109/TWC.2021.3124288

Unlike the antenna-domain channel model, which treats the wireless channel as a black box whose inputs and outputs are antenna elements, geometric and beam-space channel models [27]–[29] are more descriptive in telling what is inside the box. In the beam-space channel, inputs and outputs are beams instead of antenna elements, and they act as ports in the angular domain to which transmit power is allocated. Over this domain, the geometric model tells the distribution of those objects in the environment reflecting non-vanishing MPCs toward the receiver. IRS is one of those objects, and those spatial dimensions, or beams, overlapping with its location are utilized in its reflections. On the other hand, fading over remaining dimensions needs to be estimated not for channels with IRS but for the channel as a whole to assess other scattering clusters between transmitter and receiver. Modeling IRS in the beam-space context is essential not only for a better understanding of its behavior but also to support non-traditional antenna hardware implementations [26], where we think of the transmitting or receiving unit all as a single scattering system.

Although geometric modeling is considered for IRS-enabled channels in modeling [30], channel estimation [19], [20], and other works [5], [10], [31], they implicitly assume far-field operation and do not take into account the stationarity issue. Both near-field operation and stationarity need to be considered as IRS can be large in size [3]. However, if IRS is considered as a scattering cluster with LoS links, stationarity is not a problem as the fading in $\mathbf{F}$ and $\mathbf{G}$ need not be estimated. But still, the far-field operation assumption is impractical, and the stationarity of IRS itself at the transmitter and receiver needs to be considered. In [31], IRS is modeled differently but again as a scatterer in the far field, not a scattering cluster as done independently in this paper. Therefore, there is a need to thoroughly investigate IRS as a scattering cluster and examine the characteristics of its reflected signal regardless of its field of operation.

To fill this gap, a new channel model is proposed based on geometric and beam-space channel models. The main idea is to segment antennas into smaller parts and recognize MPC types in the channel. By segmentation, IRS behavior as a scattering cluster is clearly understood. We also show the beam sub-spaces of the whole beam-space channel and how it can be turned from a problem into a design element in the system. Segmentation eliminates the spherical wavefront issue and enables grouping segments based on the visibility regions of the scattering clusters. One main feature of the model is that the splitting based on MPC types enables the designer to select which parts of the channel to use for communication. For instance, if only the paths through IRSs are selected, there will be no need for channel estimation, but for a mobile receiver, beam training is required. Although we focus on first-order reflections by IRS, other types of reflections are also modeled and discussed. Based on the developed model, beamforming is next considered. Passive beamforming at IRS is shown to have two tiers; one at the scatterer level and the other at the antenna level with the scatterers as elements. A single-segment activation scheme at the transmitter side is proposed to maximize the received power. The number of antenna elements in this active segment is derived in a closed-form as a function of IRS angular span seen by the transmitter and beamforming at the receiver.

Different approaches are followed in the literature for path loss calculation in IRS-enabled wireless channels. The first one, as shown in [32] and [33], is based on antenna theory, where IRS is treated as an array of passive elements, each with a given radiation pattern. The overall path gain of reflected signals is found by superposing the path gains of those individual elements. The second approach is to find the electromagnetic field radiated by IRS for a given incident wave, then based on its value, path loss can be calculated at any given point [3], [34]. In [35] a circuit-based approach is adopted where IRS elements are modeled as tunable impedances to control an equivalent channel that maps voltages at transmit and receive antenna elements. The antenna-theory-based approach is followed in this paper to build the channel model.

A. Contribution

The contribution of this work is summarized in the following points:

- A classification of the scattering clusters and MPCs traveling paths in the channel is given. Also, a segmentation scheme is proposed to divide an antenna into smaller parts, called segments or scatterers. Based on the classified traveling paths, the channel is split into three sub-channels. Then, based on segmentation, the operation field issue is addressed by fitting the segments into the conventional channel models. The developed model shows clearly how the channel is controlled by IRS in the beam space.
- By segmentation, IRS is presented and investigated as a controlled scattering cluster that fits very well in the geometric model. IRS segments are equivalent to scatterers in a scattering cluster, and their gains are shown to be directly related to their phase profiles. This relation is described by what is referred to as the compensation gain.
- Based on the developed model and the segmentation scheme, the cascaded beamforming is next addressed to maximize the power delivered by IRS. A segment-activation method is proposed to eliminate phase delays due to propagation so that the received MPCs add constructively.

The rest of the paper has the following sections. Section II presents the proposed beam-space model. In Section III, IRS as a scattering cluster and its reflections are investigated. Other types of reflections are discussed in Section IV. Back to reflected signals by IRS, a cascaded beamforming scheme is proposed in Section V to maximize the received power. Also, simulations are given in this section to show the performance of the proposed solution. Finally, the paper is concluded in Section VI.

II. Channel Decomposition

In the developed model, there are three system units: transmitter T_X, receiver R_X, and IRS, denoted by L_X. Their

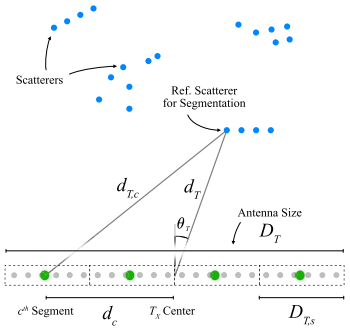

Fig. 1. Antenna segmentation.

antennas are modeled as uniform linear arrays (ULAs), where T_X (R_X or L_X) has N_T (N_R or N_L) antenna elements with antenna size D_T (D_R or D_L) and elements spacing q_T (q_R or q_L). Antenna elements are modeled as scatterers with a uniform radiation pattern in all directions except for L_X. IRS is a metasurface, and metasurfaces can be either periodic or aperiodic [3], [36]. In both cases, it is a lattice of unit cells, each with a given structure. Periodic metasurfaces have identical unit cells, and a prototype of such architecture is shown in [33]. Depending on its structure, the gain of a unit cell might not be homogeneous at all angles, so the radiation pattern of L_X elements is assumed to be of any shape and denoted by $B_{L,e}(\theta)$. As an example, it is proposed in [32], [33] to use $B_{L,e}(\theta) = a\cos^b(\theta)$ with a and b as related constants. In this work, we assume any radiation pattern for L_X elements.

A. Antenna Segmentation

Antennas can have any size and may operate in the near fields of each other. Operation fields are defined based on the approximation of the spherical wavefronts as plane wavefronts [37]. The spherical wavefront of a point source illuminating an antenna is approximated as a plane wave if it is farther than a given distance called far-field distance. This distance depends on the antenna size and the accepted maximum phase difference over its elements. For an antenna with a maximum dimension D_T, it should be more than or equal to $2D_T^2/\lambda$ for a maximum phase difference of $\pi/8$ [38].

To fit in the geometric channel model, antennas are divided into segments of elements. Similar to ordinary objects in the environment, these segments are also called scatterers. For the geometric model to be valid, scatterers with direct interaction must be in the far field of each other. Figure 1 shows an example of how to segment T_X given its distance with other scatterers. Other antennas and environment objects form a constellation of scatterers seen by T_X. The nearest scatterer acts as a reference object used to divided T_X into equal-size segments such that it will operate in their far fields. This requirement is met if

$$\min_c(d_{T,c}) \geq \frac{2D_{T,s}^2}{\lambda}, \tag{1}$$

where $d_{T,c}$ is the distance between the scatterer and the c^{th} segment whose size is $D_{T,s}$. Therefore, a segmentation that results in $D_{T,s}$ satisfying (1) is valid. The use of the segmentation method is demonstrated in the next sub-section and later sections.

B. Scatterers Splitting

The channel is assumed to be sparse with countable scatterers reflecting non-vanishing MPCs to the receiver. As shown in Fig. 2, scattering clusters in the environment are of two types: ordinary clusters (random objects in the environment) and controlled clusters (IRSs with their segments as scatterers; see Section III). Hence, the path through which an MPC travels is one of two types: homogeneous or heterogeneous. In the former, reflections of any order are due to one scatterer type; either controlled or ordinary scatterers. In the latter, reflections have a minimum order of two, and they are due to the two types of scatterers. As such, the channel matrix is decomposed into three matrices as

$$\mathbf{H} = \mathbf{H}^S + \mathbf{H}^L + \mathbf{H}^M \in \mathbb{C}^{N_R \times N_T}, \tag{2}$$

where $\mathbf{H}^S$ corresponds to the homogeneous reflections by ordinary scatterers (type-S), $\mathbf{H}^L$ corresponds to homogeneous reflections by controlled scatterers (type-L), and $\mathbf{H}^M$ corresponds to heterogeneous reflections (type-M). If we assume that the objects where IRSs are mounted have no contribution to the received signal when IRSs are uninstalled, $\mathbf{H}^S$ is the ordinary channel of the multiple-input and multiple-output (MIMO) system.

The geometric model relies on plane waves to describe the channel. It treats transmitting, receiving, and reflecting objects as scatterers and describes them by the response vectors of their incident or emitted waves at specific angles. As mentioned before, the far-field operation for those scatterers with direct interaction is necessary. Therefore, we assume that T_X and R_X are divided into S_T and S_R segments, respectively, so that any scatterer is in their far field. Consequently, the matrices in (2) are given as block matrices where

$$\mathbf{H}^y = \begin{bmatrix} \mathbf{H}^{y;1,1} & \cdots & \mathbf{H}^{y;1,S_T} \\ \vdots & \ddots & \\ \mathbf{H}^{y;S_R,1} & & \mathbf{H}^{y;S_R,S_T} \end{bmatrix} \tag{3}$$

with $y \in \{S, L, M\}$. The matrix $\mathbf{H}^{y;n,c}$, for $c = 1, \ldots, S_T$ and $n = 1, \ldots, S_R$, represents the type-y channel between the c^{th} transmitter segment, $T_{X,c}$, and the n^{th} receiver segment, $R_{X,n}$. It is modeled using the extended Saleh-Valenzuela (SV) model as follows [39]

$$\mathbf{H}^{y;n,c} = \sum_{i,j} \beta_{j,i}^{y;n,c} \mathbf{a}_{R,S}(\theta_{R,n;i,j}^y)(\mathbf{a}_{T,S}(\theta_{T,c;i,j}^y))^T \in \mathbb{C}^{N_{R,S} \times N_{T,S}}. \tag{4}$$

The j^{th} scatterer in the i^{th} cluster has a gain $\beta_{j,i}^{y;n,c}$, and the angles $\theta_{T,c;i,j}^y$ and $\theta_{R,n;i,j}^y$ describe its angular locations relative to $T_{X,c}$ and $R_{X,n}$ centers, respectively. Angular locations are with respect to the norm vector of the antenna aperture (i.e., using the broadside angle $-\pi/2 \leq \theta \leq \pi/2$). The number of antenna elements in $T_{X,c}$ and $R_{X,n}$ are $N_{T,S}$

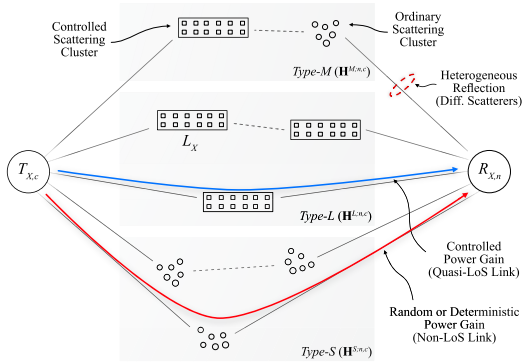

Fig. 2. Partial illustration of the geometric channel model with IRS as a controlled scattering cluster.

and $N_{R,S}$, respectively. The response vectors modeling the scatterers are given as

$$\mathbf{a}_{x,S}(\theta^{y}_{x,c;i,j}) = \left[e^{-j\gamma^{y}_{x,c;i,j}l}\right]_{l\in\mathcal{I}_{N_{x,S}}} \in \mathbb{C}^{N_{x,S}\times 1}, \tag{5}$$

where $x \in \{T, R\}$ and $c = 1, \ldots, S_x$. Given the wavelength λ and wavenumber $k = 2\pi/\lambda$, $\gamma^{y}_{x,c;i,j} = kq_x \sin(\theta^{y}_{x,c;i,j})$. Finally, the set $\mathcal{I}_z$ is defined as [40]

$$\mathcal{I}_z = \left\{ i - \frac{(z-1)}{2}; i = 0, 1, \ldots, z-1 \right\}. \tag{6}$$

The response vector for a given scatterer over the whole transmit or receive antenna is a stack of the response vectors at its segments

$$\mathbf{a}_x(\theta^{y}_{x;i,j}) = \left[\mathbf{a}_{x,S}(\theta^{y}_{x,c;i,j})\right]_{c\in\{1,\ldots,S_x\}} \in \mathbb{C}^{N_x\times 1}, \tag{7}$$

where $\theta^{y}_{x;i,j}$ is the scatterer angular location relative to x. Note that the response vector of an antenna, as one segment, is decomposed into several response vectors of smaller segments. As shown later, in this manner, the geometric model will support the spherical wavefront as we divide it into several plane wavefronts at each segment.

Unlike the conventional channel model, splitting the channel based on the traveling paths shows clearly the controlled part of the channel. As seen in Fig. 2, $\mathbf{H}^S$ delivers purely fading components and no control is possible over this sub-channel. In contrast, fully controlled components travel over the paths in $\mathbf{H}^L$. Coming between these two sub-channels is $\mathbf{H}^M$ that carries fading components affected by beamforming at IRS. The gain of a path in $\mathbf{H}^M$ is partially controlled due to the existence of ordinary scatterers; thus, it can be either deterministic or random depending on the nature of the ordinary scatterers. Finally, as it is possible to have IRS common to different paths in $\mathbf{H}^L$ and $\mathbf{H}^M$, the design of $\mathbf{H}^L$ could affect the fading in $\mathbf{H}^M$, but $\mathbf{H}^S$ is always independent of $\mathbf{H}^L$ design.

It is important to mention that segmentation does not necessarily mean an increase in the number of unknowns to be estimated. For instance, in $\mathbf{H}^L$, the goal of segmentation is always to convert the spherical wavefront into multiple plane wavefronts for the same set of scatterers. Also, note that for $S_T = S_R = 1$, the channel matrix in (3) is one-block, which is the conventional model widely used in the literature for MIMO systems. Different segmentation sizes for different scattering clusters are possible. For example, ordinary scattering clusters between T_X and R_X might all operate in the far fields, but there is an IRS in the near field. In such case, $S_T = S_R = 1$ for $\mathbf{H}^S$, but multiple segments are required at T_X and R_X for $\mathbf{H}^L$.

The model in (4) is for frequency-flat fading channels; however, the extension to frequency-selective channels is possible using OFDM-based precoding and combining [41]. In this case, the same model applies but for individual subcarriers. Similar to analog beamforming at T_X and R_X sides, the same passive beamforming at IRS applies to all subcarriers.

C. Scatterers Gains

The gains applied to MPCs reflected by ordinary scatterers, $\{\beta^S_{i,j}\}$, are widely modeled stochastically with a given distribution. However, other methodologies are followed in channel modeling to include MPCs, other than the LoS component, with deterministic power gains [21]. For instance, the IEEE 802.11ay channel model [42] follows this quasi-deterministic approach to model the mmWave channel with different types of MPCs. One type is called D-ray, and it is found based on ray-tracing reconstruction for a given scenario environment. It is an MPC reflected from a macro object with possibly added random MPCs to form a quasi-deterministic MPC. Another type is called R-ray and it represents reflections from random objects. This type of MPCs is random and follows the complex Gaussian distribution. On the other hand, as shown in later sections, $\{\beta^L_{i,j}\}$ are controlled by means of passive beamforming at L_X side, and they are always deterministic for known T_X and R_X locations.

Ordinary scattering clusters reflect signals with an uncontrolled gain that depends on their composition, but signals reflected by IRS are optimized in the sense that reflected MPCs can be focused to maximize the received power. Also, IRS gives a degree of control over those reflected MPCs. For example, it can direct the incident signal into different directions, which is a feature that is not possible by ordinary scattering clusters. However, optimizing IRS reflections requires accurate-enough knowledge of its location relative to T_X and R_X. For point-to-point communication with fixed T_X and R_X locations, as in backhaul communication, this might be a valid assumption. However, in the case of having mobile R_X, a (beam) training stage is required to compensate for phase differences between reflected MPCs.

D. Beam Subspaces

Figure 3 shows how geometric and beam-space channel models fit together. Beamforming at $T_{X,c}$ or $R_{X,n}$ side is approximated by selection windows in the angular domain. The output of a window is one resolvable MPC, which is a combination of unresolvable physical MPCs [43]. (Here, we might also call a group of physical MPCs as one physical MPC.) It is also shown in the figure how IRS acts similar to other clusters by reflecting multiple MPCs, which are not random but controlled as shown later in Section III.

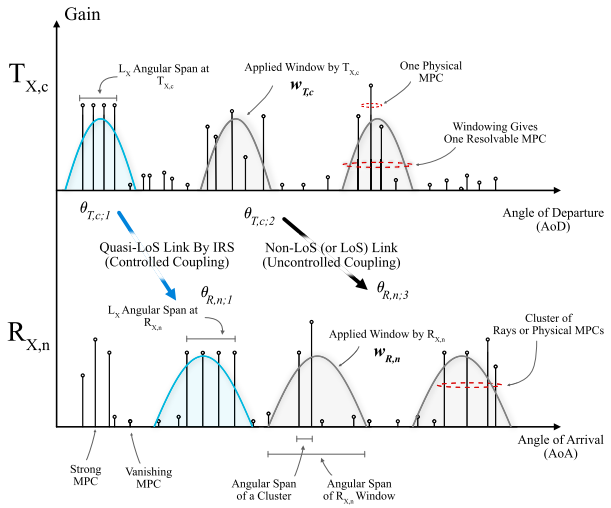

Fig. 3. Beam-space channel model with IRS as a source of cluster of MPCs.

Similar to response vectors, beamforming vectors are decomposed into smaller vectors for individual segments. Hence, for a given segment, the beam-space beamforming vector [40] is

$$\mathbf{w}_{x,S}(\theta_{x,c,S}) = \frac{1}{\sqrt{N_x}}\left[e^{j\gamma_{x,c,S}l}\right]_{l\in\mathcal{I}_{N_{x,c}}} \in \mathbb{C}^{N_{x,c}\times 1}, \quad (8)$$

where $\gamma_{x,c,S} = kq_x \sin(\theta_{x,c,S})$ with $\theta_{x,c,S}$ as the segment steering angle. This vector corresponds to a beam that acts as a selection window applied by the segment to select a specific angular span as shown in Fig. 3. Physical MPCs within a window go under different beamforming gains depending on the beam shape, and the gain at directions outside the window is small enough to be neglected.

The beamforming vector over the whole transmit or receive antenna is given as

$$\mathbf{w}_x = \left[\mathbf{w}_{x,S}(\theta_{x,c,S})\right]_{c\in\{1,\ldots,S_x\}} \in \mathbb{C}^{N_x\times 1}. \quad (9)$$

For multiple RF chains, the analog beamforming matrix is given as

$$\mathbf{W}_x = \left[\mathbf{w}_x^1, \mathbf{w}_x^2, \ldots, \mathbf{w}_x^{M_x}\right] \in \mathbb{C}^{N_x\times M_x} \quad (10)$$

where $\mathbf{w}_x^i$ is the i^{th} beamforming vector as given in (9) and M_x is the number of RF chains.

The beam-space channel matrix is given as

$$\begin{aligned}\mathbf{H}_B &= (\mathbf{W}_R)^T\mathbf{H}\mathbf{W}_T \\ &= (\mathbf{W}_R)^T\mathbf{H}^L\mathbf{W}_T + \mathbf{H}_B^I \in \mathbb{C}^{M_R\times M_T}\end{aligned} \quad (11)$$

Unlike $\mathbf{H}$ in (3), $\mathbf{H}_B$ is not a block matrix, but its internal structure, based on $\mathbf{H}$ and $\mathbf{W}_x$, is a composition of block matrices. In the conventional beam-space channel, the matrix elements represent coupling between one pair of beams. But in $\mathbf{H}_B$ here, they represent coupling between one pair of composite beams. One such beam has multiple beams stemming from antenna segments. Segments beams are unresolvable in $\mathbf{H}_B$, though they can be controlled at T_X and R_X sides. The control is possible by steering the beam (beamforming) or changing its size (segmentation), but once T_X sends a beam into the channel, it is not controlled unless it is sent through a homogeneous path of controlled scattering clusters. *Therefore, by L_X in the beam space, complete control of the information-carrying signal from source to destination is possible with almost no randomness.* In other words, L_X converts the channel from a problem to a design element in the wireless communication system. This is shown clearly by the second line of (11), where $\mathbf{H}^L$ is singled out as a controlled part of the geometric channel while other parts are left in $\mathbf{H}_B^I$ as an interference source in the beam-space channel. A designer might consider beamforming design and IRSs distribution in the environment to suppress $\mathbf{H}_B^I$ while maintaining the IRS-enabled channel part for communication. Such an approach can eliminate the need for channel estimation, but it might give rise to the need for beam training, mainly at L_X, to maximum reflected signal power. In Section V, the two-tier nature of passive beamforming at L_X explains this clearly, but first, we show how L_X acts as a controlled scattering cluster in the next section.

III. IRS as Scattering Cluster

In this section, $\mathbf{H}^L$ in (2) is further investigated, where we study the gains of MPCs reflected by L_X with a focus on first-order reflections. We assume a single IRS in the channel, and the locations of T_X and R_X relative to L_X are known.

We start with segmenting the system units. As shown in Fig. 4, T_X interacts with L_X only, so it is segmented based on its nearest scatterer at L_X, where we consider each L_X element as a scatterer. This reference scatterer happened to be the edge element in this example and based on (1), we find the maximum T_X segment size using its distance with the closest segment, which is $d_{T,\text{seg}}$. The same applies to R_X. On the other hand, L_X interacts with both T_X and R_X, so it is segmented based on the distances with their elements. In this example, it happened to have the reference scatterer at T_X. With the obtained segments as scatterers, L_X is presented next as a controlled scattering cluster.

A. IRS Multipath Components

Consider the channel $\mathbf{H}^{L;n,c}$ between $T_{X,c}$ and $R_{X,n}$, and assume S_L segments at L_X. Let the distance between the m^{th} L_X segment, $L_{X,m}$, and $T_{X,c}$ (or $R_{X,n}$) be $d_{T,c;m}$ (or $d_{R,n;m}$). The channel response from T_X to R_X is given as

$$\begin{aligned}&\mathbf{H}^{L;n,c} \\ &= \sum_{m=1}^{S_L} \rho_{m;c,n}\mathbf{a}_{R,S}(\theta_{R,n;m})(\mathbf{a}_{L,S}(\theta_{L,m;R,n}))^T \\ &\quad\times \mathbf{\Phi}_m\mathbf{a}_{L,S}(\theta_{L,m;T,c})(\mathbf{a}_{T,S}(\theta_{T,c;m}))^T \in \mathbb{C}^{N_{R,S}\times N_{T,S}},\end{aligned} \quad (12)$$

where $\mathbf{a}_{T,S}(\theta)$, $\mathbf{a}_{L,S}(\theta)$ and $\mathbf{a}_{R,S}(\theta)$ are the channel response vectors at $T_{X,c}$, $L_{X,m}$ and $R_{X,n}$, respectively, as defined in (5). The angles $\theta_{T,c;m}$ and $\theta_{R,n;m}$ are the locations of $L_{X,m}$ with respect to the center of $T_{X,c}$ and $R_{X,n}$, respectively. On the other hand, $\theta_{L,m;T,c}$ and $\theta_{L,m;R,n}$ are the locations

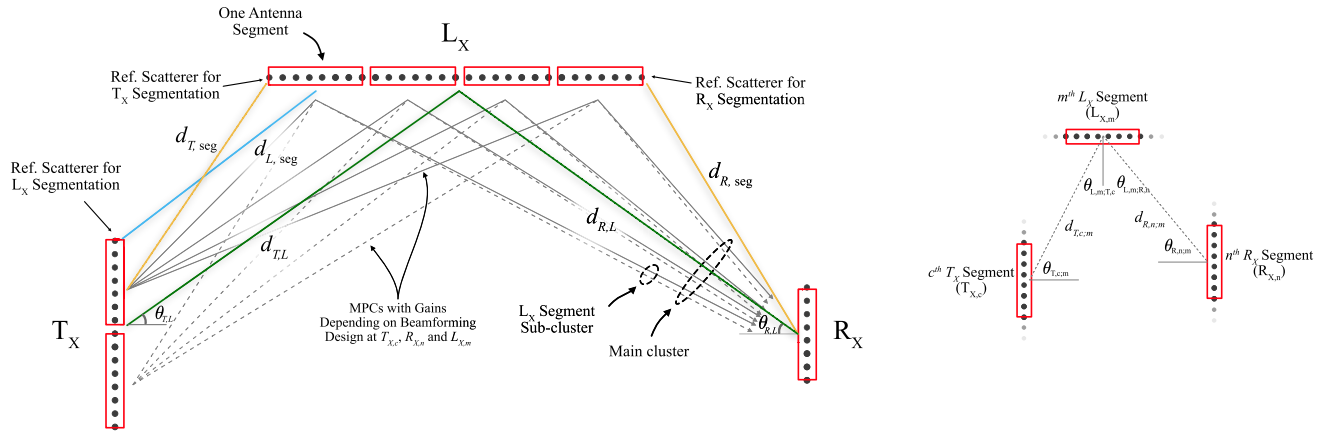

Fig. 4. Antennas segments with their corresponding MPCs.

of $T_{X,c}$ and $R_{X,n}$, respectively, relative to the center of $L_{X,m}$ (See Fig. 4). The propagation coefficient given by

$$\rho_{m;c,n} = \frac{e^{jk(d_{T,c;m}+d_{R,n;m})}}{b_{\text{att}}^2 (d_{T,c;m} d_{R,n;m})^{a_{\text{att}}/2}} \tag{13}$$

describes path loss and phase delay due to propagation, where a_{att} is the path-loss exponent and b_{att} is a model-dependent constant. For free-space propagation, we have $a_{\text{att}} = 2$ and $b_{\text{att}} = 2k$. Finally, the matrix

$$\mathbf{\Phi}_m = diag(e^{j\phi_{m,1}}, \ldots, e^{j\phi_{m,N_{L,S}}}) \in \mathbb{C}^{N_{L,S} \times N_{L,S}} \tag{14}$$

represents the phases applied by $L_{X,m}$, where $\phi_{m,i}$ is the phase introduced by its i^{th} element.

The term

$$\alpha_{m;c,n} = (\mathbf{a}_{L,S}(\theta_{L,m;R,n}))^T \mathbf{\Phi}_m \mathbf{a}_{L,S}(\theta_{L,m;T,c}) \tag{15}$$

is a scalar and called the *compensation gain* of $L_{X,m}$ at $R_{X,n}$ for $T_{X,c}$ signal reflection, which depends on the segment passive beamforming design as shown in Section V. If we define $B_{m;c,n} = B_{L,e}(\theta_{L,m;T,c}) B_{L,e}(\theta_{L,m;R,n})$, then by writing the MPC gain as

$$\beta_m^{L;n,c} = B_{m;c,n} \rho_{m;c,n} \alpha_{m;c,n}, \tag{16}$$

the channel in (12) can be written as

$$\mathbf{H}^{L;n,c} = \sum_{m=1}^{S_L} \beta_m^{L;n,c} \mathbf{a}_{R,S}(\theta_{R,n;m}) (\mathbf{a}_{T,S}(\theta_{T,c;m}))^T, \tag{17}$$

which matches with the definition given in (4) for a single scattering cluster, and it is the case when T_X and R_X have a small enough number of antenna elements so that any L_X element operates in their far field. It is mainly the case of conventional MIMO systems. Based on this result, the following comments are given:

- IRS acts similar to ordinary scattering clusters; it is a collection of scatterers called segments. One MPC stems from each segment; however, unlike those stem from ordinary scatterers, its gain is known and controlled.
- Equation (17) emphasizes IRS as a means to control the channel and signal propagation through it. As part of the channel, the gains of its reflected MPCs depend on its beamforming design. This is in contrast to beamforming at T_X or R_X, which does not alter the channel but gives a response to it.
- The minimum number of segments, or controlled scatterers, is governed by the largest permissible segment size found by (1). More segments might be assumed, but their number does not exceed N_L, where one segment is an individual element.

Additional segments at T_X means additional MPCs reflected by L_X with a total of $S_T S_L$ MPCs, as shown in the example in Fig. 4. Every S_T MPCs reflected by $L_{X,m}$ are controlled as one group or sub-cluster and cannot be distinguished by $L_{X,m}$. At R_X, having additional segments means receiving the $S_T S_L$ MPCs by S_R segments with different gains. In general, the $S_T S_L S_R$ scatterers in $\mathbf{H}^L$ as given by (3) and (4) are dependent and correspond to the same S_L scatterers but at different angles. *As a result, only the change in L_X segments changes the channel.* The scatterer drifting in angular domains seen by adjacent segments results in different gains of its reflected signal toward those segments, and differences are expressed by the compensation gains. The following sub-section reveals what is the MPC reflected by IRS in the beam-space context. But as a short answer, it is a weighted beam(s); more precisely, it is a cascade of plane waves.

B. Geometric Interpretation

In the conventional beam-space channel, the beamforming design given in (8) is adopted, but T_X is one segment. For a steering angle $\theta_{T,S}$, the normalized field signal of T_X at an angle θ_T is given as

$$\begin{aligned} B_T(\theta_T; \theta_{T,S}) &= g_0 (\mathbf{a}_T(\theta_T))^T \mathbf{w}_T \\ &= \frac{g_0}{\sqrt{N_T}} \sum_{l \in \mathcal{I}_{N_T}} e^{j(\gamma_{T,S} - \gamma_T)l} \\ &= \frac{g_0}{\sqrt{N_T}} f(\gamma_T - \gamma_{T,S}; N_T), \end{aligned} \tag{18}$$

where $g_0 = e^{jkd_T}/(d_T)^{a_{\text{att}}/2}$, and for the rest of the paper, we define $\gamma_{X,y} = kq_X \sin(\theta_{X,y})$ for $X \in \{T, R, L\}$ and any y. The function $f(\theta; N)$ is known as the Dirichlet kernel [44]

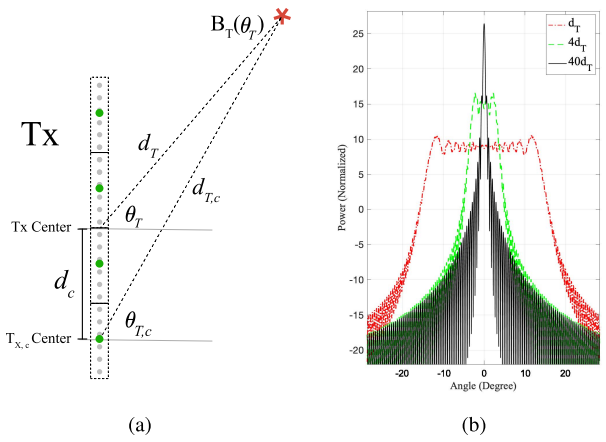

(a) (b)

Fig. 5. The beam convergence over distance.

and it is an even function defined as

$$f(\theta; N) = \sum_{l \in \mathcal{I}_N} e^{-j\theta l} = \frac{\sin(N\theta/2)}{\sin(\theta/2)}, \tag{19}$$

We say that $f(\theta - \theta_o; N)$ has a size N and is centered at θ_o, which means its main lobe with a width $4\pi/N$ is directed toward θ_o.

In the near field, the field signal is calculated using the response vectors of individual segments. As shown in Fig. 5(a), a point located at distance d_T and angle θ_T with respect to T_X center is located at $\theta_{T,c}$ and distance $d_{T,c}$ with respect to $T_{X,c}$ center. For the same conventional beamforming design as in (18), we note that each segment beamforming vector has the same steering angle value ($\theta_{T,c,S} = \theta_{T,S} \forall c$), but there is a common phase applied to all its elements. Its value is $c\gamma_{T,S}N_{T,S}$ for $T_{X,c}$. The normalized field signal now might be expressed as

$$B_T(\theta_T; \theta_{T,S}) = \sum_{c \in \mathcal{I}_{S_T}} \underbrace{(g'_c \mathbf{a}_{T,S}(\theta_{T,c}))^T}_{\text{Channel Response}} \underbrace{\mathbf{w}_{T,S}(\theta_{T,S}) e^{-jc\gamma_{T,S}N_{T,S}}}_{\text{Beamforming Vector}} \tag{20}$$

where $g'_c = e^{jkd_{T,c}}/(d_{T,c})^{a_{\text{att}}/2}$. Similar to beamforming vectors, we notice that the channel response has the same two-tier feature, where each segment has a common phase delay to all its elements due to propagation.

After simple manipulations, we get

$$B_T(\theta_T, \theta_{T,S}) = \sum_{c \in \mathcal{I}_{S_T}} g_c f(\gamma_{T,c} - \gamma_{T,S}; N_{T,S}), \tag{21}$$

where $g_c = g'_c e^{-jc\gamma_{T,S}N_{T,S}}/\sqrt{N_T}$. The above equation suggests treating each antenna segment as an independent source, which is the approach followed in this work. The field signal at a given point in the space is a superposition of weighted kernels of size $N_{T,S}$. It can be easily found that (21) converges to (18) as $d_T \to \infty$. Figure 5(b) shows how the beam evolves over distance as the kernels converge to one beam that is independent of distance.

Assume having only one $T_{X,c}$ in (21) and ignore its phase delay and path loss for now. Based on the kernel definition in (19), $T_{X,c}$ acts as a source of $N_{T,S}$ plane waves arriving $L_{X,m}$ at the same angle $\theta_{L,m;T,c}$ as shown in Fig. 6. Each plane wave can be thought of as a virtual source (i.e. single RF chain and its phase-shifting circuit) connected to $L_{X,m}$ elements and set to a steering angle $-\theta_{L,m;T,c}$, given that $\mathbf{\Phi}_m = \mathbf{I}_m$, where $\mathbf{I}_m$ is an identity matrix of size m. However, the steering angle can be controlled by $\mathbf{\Phi}_m$. For instance, if it is desired to direct the reflected beam toward θ_{L,m_o}, the phases are set such that $\phi_{m,i} = \zeta_m i$ where $\zeta_m = \gamma_{L,m;T,c} + \gamma_{L,m_o}$. Thus, the reflected field signal, while ignoring the radiation pattern, is given as

$$\begin{aligned} &B_{L,m;c}(\theta_{L,m}) \\ &= \sum_{l \in \mathcal{I}_{N_{T,S}}} \frac{e^{j(\gamma_{T,S} - \gamma_{T,c;m})l}}{\sqrt{N_T}} f(\gamma_{L,m} + \gamma_{L,m;T,c} - \zeta_m; N_{L,S}) \\ &= \alpha_{T,c;m} f(\gamma_{L,m} + \gamma_{L,m;T,c} - \zeta_m; N_{L,S}) \end{aligned} \tag{22}$$

where $\theta_{L,m}$ is the angle with respect to $L_{X,m}$ center and $\alpha_{T,c;m} = f(\gamma_{T,S} - \gamma_{T,c;m}; N_{T,S})/\sqrt{N_T}$ is the compensation gain of $T_{X,c}$ at $L_{X,m}$, which is defined in a similar manner to that for $L_{X,m}$ in (15). Note that in the conventional beam-space channel, each system unit has one segment, so we have one compensation gain that can be maximized to have $\alpha^2_{T,c;m} = N_{T,S} = N_T$. However, in near-field operation, L_X might have multiple segments, and only one $L_{X,m}$ can have a maximum compensation gain.

Based on (22), we note that the reflected signal by $L_{X,m}$ is also a kernel. Therefore, the kernel at $T_{X,c}$ is equivalent to another one at $L_{X,m}$ but with different size, allowing for more design freedom (by having T_X spanning angular domains of two different locations at the same time!)

The received signal by $R_{X,n}$ is a stack of clustered plane waves as seen in Fig. 6. To obtain maximum gain at $R_{X,n}$, it is necessary, but not sufficient, to compensate their phase differences. Each cluster has replicas of a plane wave received by $L_{X,m}$ from one element at $T_{X,c}$. Therefore, their phase differences are compensated by active beamforming at T_X, while phase differences between the clusters themselves is compensated by the passive beamforming at $L_{X,m}$.

In case of having multiple segments at T_X, each of them corresponds to an additional kernel reflected by $L_{X,m}$ at its own angle $-\theta_{L,m;T,c}$. Based on (21) and (22), the reflected signal by $L_{X,m}$ due to signals received from multiple segments at T_X with the same steering angle is given as

$$B_{L,m}(\theta_{L,m}) = \sum_{c \in \mathcal{I}_{S_T}} \sqrt{N_{T,S}} g_c B_{L,m;c}(\theta_{L,m}). \tag{23}$$

Steering at $L_{X,m}$ is applied to all its kernels as one group, and it is not possible to steer them individually. The total reflected signal by L_X can be found in a similar manner to the derivation of (21), where segments signals as defined in (23) can be controlled independently.

As a summary, in conventional beam-space modeling, T_X with one RF chain is designed to give one beam in a given direction. On the other hand, L_X gives $S_T S_L$ weighted kernels with a size that depends on the segment size. Every segment at L_X reflects S_T kernels and the difference between their angular directions depends on T_X segments angular locations

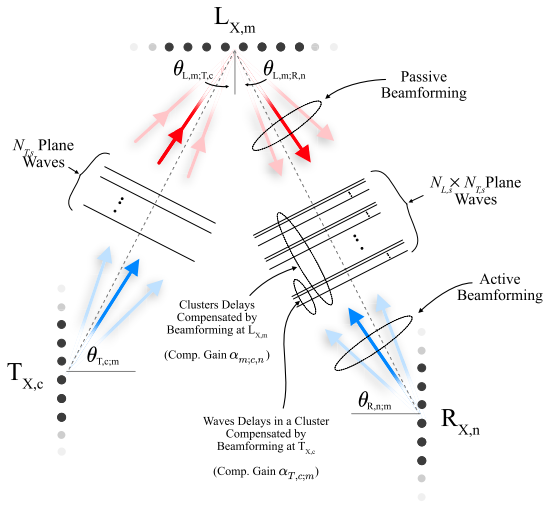

Fig. 6. Type-L reflections.

with respect to $L_{X,m}$. Thus, T_X segments are equivalent to S_T virtual sources connected to $L_{X,m}$ each with its own default steering angle $-\theta_{L,m;T,c}$. From a stationarity perspective, IRS as a scattering cluster is seen at slightly different angles by T_X segments. If L_X is in the far field of T_X and R_X (i.e., each has one segment), the reflected signal by $L_{X,m}$ will be a single beam. Moreover, if T_X and R_X are in the far field of L_X, it acts as one scatterer with a single DK, which the case adopted in works like [10], [31]. Finally, the number of reflected kernels by L_X increases by choosing smaller segment size; however, each new one will have a wider span and less reflected power.

IV. Other Reflections

In previous sections, we focused on $\mathbf{H}^L$ with first-order reflections. In this section, higher-order reflections in $\mathbf{H}^L$ and other types of paths in (2) are discussed by following the same segmentation approach.

A. Type-S Reflections

Two problems that arise for large antennas are non-stationarity and spherical wavefront [21]. Implicitly, these problems were addressed for reflections by L_X. Ordinary scattering clusters, on the other hand, are not (or less) controlled and might not exist across the entire antenna [45]. Consequently, the blocks in $\mathbf{H}^S$ might not have the same set of scatterers. Based on the concept of visibility regions [45], a cluster is common to a group of antenna elements if they fall in its visibility region. Therefore, ordinary scattering clusters exist in $\{\mathbf{H}^{S,n,c}\}$ based on their visibility regions. For the statistical modeling of visibility regions, [21], [45], [46], and references therein might be consulted.

For a scatterer common to a large portion of the antenna, the spherical wavefront issue arises, and in the literature, it is addressed by modifying the response vectors to include phase delays due to the wave shape as shown in [46]. In [46], also an approximation for the wave by a parabolic wavefront is given. Unlike spherical and parabolic wavefronts, segmentation maintains the connection between the geometric and beam-space models with the new interpretation discussed earlier by replacing the spherical wavefront with multiple plane wavefronts. Segmentation does not require the exact distance with a scatterer. It is possible to segment based on a distance below which no scattering clusters exist, but this distance should be scenario-dependent as it can be different for different environments.

B. Higher-Order Reflections

The extension to higher-order reflections in $\mathbf{H}^L$ is as follows. As the extension to other orders follows similarly, we assume a second-order reflection by IRSs. The first IRS, L_{X1}, has interaction with T_X and the second IRS, L_{X2}, while L_{X2} interacts with R_X and not T_X. Therefore, L_{X1} is segmented into S_{L1} segments based on its distances with T_X and L_{X2}, and L_{X2} is segmented into S_{L2} segments based on its distances with L_{X1} and R_X. The number of segments at both IRSs is chosen as $S_L = \max(S_{L1}, S_{L2})$. The same channel model in (4) applies to the path with two IRSs as if they are one virtual IRS with S_L segments. The angles $\{\theta^L_{T,c;i,j}\}$ represent the locations of L_{X1} segments with respect to $T_{X,c}$, and $\{\theta^L_{R,n;i,j}\}$ are the locations of L_{X2} segments with respect to $R_{X,n}$. As each scatterer at L_{X2} reflects signals coming from all scatterers at L_{X1}, the gains are given as

$$\beta^{L;n,c}_{i,j} = \sum_{k=1}^{S_L} \beta^{L;n,c}_{i,j,k} \tag{24}$$

where $\beta^{L;n,c}_{i,j,k}$ is the gain of the path from $T_{X,c}$ to $R_{X,n}$ through the k^{th} and j^{th} segments at L_{X1} and L_{X2}, respectively, which can be easily found by following the approach in Section III-A.

The heterogeneous paths in $\mathbf{H}^M$ give at least second-order reflections. Assume a second-order reflection, for simplicity, where there are two cascaded scattering clusters, one is ordinary and the other is controlled. As discussed above, it is possible to have a group of L_X segments in the visibility region of the ordinary cluster. Only this subset of L_X segments will contribute to $\mathbf{H}^M$. Steering vectors are defined similar to second-order reflections by IRSs; however, the gain of a path through the j^{th} segment at L_X and i^{th} ordinary scatterer will be $\beta^{M,n,c}_{i,j} = \beta'_{i,j}\beta^{L,n,c}_{i,j}$, where $\beta'_{i,j}$ is the ordinary scatterer gain and $\beta^{n,c}_{L,i,j}$ is the segment gain as defined in (16) but with respect to the scatterer and not $T_{X,c}$.

V. Cascaded Beamforming

Near-field beamforming to maximize the received signal power at R_X through L_X quasi-LoS link is addressed in this section. We assume analog beamforming at both T_X and R_X sides and that R_X has only one segment. Also, we focus back on first-order reflection by IRS.

A. Problem Formulation

By considering one IRS only in the environment, the channel between the $T_{X,c}$ and R_X is given based

on (17) as

$$\mathbf{H}^{L;c} = \sum_{m=1}^{S_L} \beta_m^{L;c} \mathbf{a}_R(\theta_{R;m})(\mathbf{a}_{T,S}(\theta_{T,c;m}))^T. \quad (25)$$

As we focus on received power maximization, assume a unity transmitted signal with no information. Then, the received signal after combining is given based on (11) as

$$\begin{aligned} r &= (\mathbf{w}_R)^T \sum_{c=1}^{S_T} \mathbf{H}^{L;c} \mathbf{w}_{T,c}, \\ &= \sum_{m=1}^{S_L} \sum_{c=1}^{S_T} \beta_m^{L;c} (\mathbf{w}_R)^T \mathbf{a}_R(\theta_{R;m})(\mathbf{a}_{T,S}(\theta_{T,c;m}))^T \mathbf{w}_{T,c}, \end{aligned} \quad (26)$$

where $\mathbf{w}_{T,c} = [w_{T,c,i}]_{i \in \mathcal{I}_{N_{T,S}}}$ and $\mathbf{w}_R = [w_{R,i}]_{i \in \mathcal{I}_{N_R}}$ are the beamforming vectors of $T_{X,c}$ and R_X, respectively. Therefore, the beamforming problem is given as

$$\begin{aligned} \mathbf{\Gamma} = \arg\max_{\mathbf{\Gamma}} & |r|^2 \\ \text{s.t. } & |w_{R,i}|, |w_{T,c,i}| = 1; \quad \forall i \end{aligned} \quad (27)$$

where $\mathbf{\Gamma} = \{\mathbf{w}_{T,c}, \mathbf{w}_R, \mathbf{\Phi}_m\}_{m,c}$ is the beamforming parameters vector.

We have two beamforming levels. Tier-1 beamforming is for the segments themselves and it is based on the design in (5). The second one is for the antenna with segments as its elements, and it is represented by a common phase applied to all segment elements. Therefore, we have

$$\mathbf{w}_{T,c} = \mathbf{w}'_{T,S}(\theta_{T,c,S}) e^{j\phi_{T,c}} \quad (28)$$

$$\mathbf{w}_R = \mathbf{w}'_R(\theta_{R,S}) e^{j\phi_R} \quad (29)$$

where $\mathbf{w}'_{T,S}$ and $\mathbf{w}'_R$ are based on the design in (5). For segment x, where $x \in \{(T,c), R\}$, $\theta_{x,S}$ is the steering angle for tier-1 beamforming and ϕ_x is its applied phase for tier-2 beamforming. The compensation gains at $T_{X,c}$ and R_X are given respectively as

$$\begin{aligned} \alpha_{T,c;m} &= (\mathbf{a}_{T,S}(\theta_{T,c;m}))^T \mathbf{w}'_{T,S}(\theta_{T,c,S}) \\ &= f(\gamma_{T,c,S} - \gamma_{T,c;m}; N_{T,S})/\sqrt{N_T}, \end{aligned} \quad (30)$$

and

$$\begin{aligned} \alpha_{R;m} &= (\mathbf{w}'_R(\theta_{R,S}))^T \mathbf{a}_R(\theta_{R;m}) \\ &= f(\gamma_{R,S} - \gamma_{R;m}; N_R)/\sqrt{N_R}. \end{aligned} \quad (31)$$

By following the same design for passive beamforming, the phase shifts introduced by $L_{X,m}$ are given by

$$\mathbf{\Phi}_m = \mathbf{\Phi}'_m e^{j\phi_{L,m}} \quad (32)$$

where, for a passive steering angle $\theta_{L,m,S}$, $\mathbf{\Phi}'_m = diag(\dots, e^{j\gamma_{L,m,S}l}, \dots)_{l \in \mathcal{I}_{N_{L,S}}}$ and $\phi_{L,m}$ is the applied phase for second-tier beamforming. Based on (15), two responses are given for reflection and the compensation gain of $L_{X,m}$ is given as

$$\alpha_{m;c} = f(\gamma_{L,m,S} - (\gamma_{L,m;R} + \gamma_{L,m;T,c}); N_{L,S}). \quad (33)$$

Note that unlike steering angles at $T_{X,c}$ and R_X, the passive steering angle is not necessarily the same angle towards which the signal is directed.

By ignoring the radiation pattern effect and attenuation due to propagation in (16), the problem given in (27) is equivalent to

$$\begin{aligned} \mathbf{\Omega} = \arg\max_{\mathbf{\Omega}} & \Big| \sum_{m=1}^{S_L} \sum_{c=1}^{S_T} g_{c,m} e^{jp_{c,m}} \Big|^2 \\ \text{s.t. } & |\gamma_{T,c,S}| \le kq_T, \quad |\gamma_{R,S}| \le kq_R, \ |\gamma_{L,m,S}| \le kq_L, \end{aligned} \quad (34)$$

where $\mathbf{\Omega} = \{\gamma_{T,c,S}, \gamma_{R,S}, \gamma_{L,m,S}, \phi_{T,c}, \phi_{L,m}\}_{m,c}$ is the new parameters vector and

$$g_{c,m} = \alpha_{T,c;m} \alpha_{R;m} \alpha_{m;c}, \quad (35)$$

$$p_{c,m} = k(d_{R;m} + d_{T,c;m}) + \phi_{T,c} + \phi_{L,m}. \quad (36)$$

The phase ϕ_R is omitted from (36) as it is independent of the summation indices in (34). We note that the received signal is a combination of $S_T S_L$ MPCs (as illustrated in Fig. 4), each has magnitude and phase depending on tier-1 and tier-2 beamforming designs, respectively.

B. Single-Segment Activation

Unlike segments at L_X and R_X, those at T_X can be switched on and off by means of power allocation. For fixed S_T and $N_{T,s}$, an optimum design leads to no better than maximized gains and completely compensated phase delays for the MPCs in (34). Obviously, this is possible when each system unit has one segment (i.e., far-field operation). It is the case of conventional far-field beamforming, where compensation gains are maximized as each beam is focused toward one segment only, and there is one MPC, the phase of which can be compensated at any segment.

Changing S_T and $N_{T,S}$ affects $g_{c,m}$ and $p_{c,m}$. As phases have serious impact on the received signal power, the proposed solution next focuses on complete compensation for their effect. Based on (34) and (36), we have a total of $S_T S_L$ MPCs, each with its own phase delay $k(d_{R;m} + d_{T,c;m})$ due to propagation. However, for tier-2 beamforming we have $(S_T + S_L + 1)$ degrees of freedom for phase compensation. Therefore, for a complete phase delay compensation, it is required to have $S_T + S_L + 1 \ge S_T S_L$. To meet this requirement, a single-segment activation method is proposed where only one segment at T_X is activated by allocating the transmission power only to its elements. Therefore, we have $N_{T,s} = N_T$, and for notational simplicity, the subscript T, c is replaced by T.

By changing the number of active elements at T_X, we introduce a new optimization variable to the problem in (34), which is their number $N_{T,S}$. Therefore, the new problem is given as

$$\begin{aligned} &\{\mathbf{\Omega}, N_{T,S}\} \\ &= \arg \max_{\{\mathbf{\Omega}, N_{T,S}\}} \Big| \sum_{m=1}^{S_L} g_m e^{jp_m} \Big|^2 \\ &\quad \text{s.t. } |\gamma_{T,S}| \le kq_T, \ |\gamma_{R,S}| \le kq_R, \ |\gamma_{L,m,S}| \le kq_L, \\ &\quad N_{T,S} \le N_o, \end{aligned} \quad (37)$$

where N_o is the maximum number of elements of a T_X segment centered at the antenna center. Given one segment

at T_X and R_X, we have

$$g_m = N_{L,S}\alpha_{T;m}\alpha_{R;m}, \tag{38}$$

$$p_m = k(d_{T;m} + d_{R;m}) + \phi_{L,m}. \tag{39}$$

In comparison with (35), we note that $\alpha_{m;c}$ is replaced by its maximum value as we choose

$$\gamma_{L,m,S} = \gamma_{L,m;T} + \gamma_{L,m;R} \quad \forall m. \tag{40}$$

Similar to ϕ_R exclusion from (36), the tier-2 phase at T_X is omitted from (39) as it is independent of the summation index in (37). It can be seen clearly in (39) that phase delays are completely compensated by setting tier-2 phases at L_X segments such that

$$\phi_{L,m} = -k(d_{T;m} + d_{R;m}) \quad \forall m. \tag{41}$$

Based on the design above, tier-1 and tier-2 beamforming at L_X are optimum for the proposed scheme. On the other hand, there is no tier-2 beamforming at T_X and R_X, and their compensation gains at L_X segments have some losses depending on their steering angles. As the power captured by R_X is mostly at directions close to its steering angle forming the main lobe of its beam, we neglect compensation gains outside the main lobe by defining the approximation

$$\alpha'_{R;m} = \begin{cases} \alpha_{R;m}; & |\gamma_{R,S} - \gamma_{R,m}| \le 2\pi/N_R \\ 0; & \text{otherwise.} \end{cases} \tag{42}$$

By adopting the main-lobe approximation given in Appendix, we might proceed in solving the beamforming problem by addressing the following problem

$$\begin{aligned} \{\mathbf{\Omega}', N_{T,S}\} = \arg \max_{\{\mathbf{\Omega}', N_{T,S}\}} & \sum_{m=1}^{S_L} \alpha'_{T;m}\alpha'_{R;m} \\ \text{s.t. } & |\gamma_{T,S}| \le kq_T, \quad |\gamma_{R,S}| \le kq_R, \\ & N_{T,S} \le N_o, \end{aligned} \tag{43}$$

where $\mathbf{\Omega}' = \{\gamma_{T,S}, \gamma_{R,S}\}$ and

$$\alpha'_{T,m} = f_{\text{approx}}(\gamma_{T,s} - \gamma_{T,m}; N_{T,S})/\sqrt{N_{T,S}}. \tag{44}$$

For a given $N_{T,S}$, steering angles are chosen based on averaging to minimize the compensation lose, so

$$\gamma_{T,S} = \langle \gamma_{T;m} \rangle_m, \tag{45}$$

$$\gamma_{R,S} = \langle \gamma_{R;m} \rangle_m, \tag{46}$$

where $\langle \cdot \rangle_m$ is the averaging operator over the index m. Given $\gamma_{T,S}$, $N_{T,S}$ is found based on the derivative of the objective function of the problem in (43) such that

$$\begin{aligned} \sum_{m=1}^{S_L} \frac{\alpha'_{R;m}}{2\sqrt{N_{T,S}}} \left[1 - \frac{5N_{T,S}^2 - 1}{24} \left(\gamma_{T,S} - \gamma_{T;m} \right)^2 \right] \\ \approx \frac{1}{2\sqrt{N_{T,S}}} \left[C_0 - \frac{C_1}{5} N_{T,S}^2 \right] = 0. \end{aligned} \tag{47}$$

Therefore, the value of $N_{T,S}$ that satisfies (47) is given as

$$N_{T,S} = \sqrt{\frac{5C_0}{C_1}}, \tag{48}$$

where

$$C_0 = \sum_{m=1}^{S_L} \alpha'_{R;m} \tag{49}$$

$$C_1 = \sum_{m=1}^{S_L} \alpha'_{R;m} \left(\gamma_{T,S} - \gamma_{T;m} \right)^2. \tag{50}$$

It is important to note that the active segment size depends on the angular span of L_X and beamforming at R_X, where the compensation gain of R_X at an L_X segment weights its importance in power reflection. To understand this dependency, consider the following cases with $S_L = N_L$ (i.e., each element at L_X is a segment by itself). By ignoring the operating fields, the first one is for $N_R \to \infty$, where its compensation gain will be maximum at only one L_X segment and goes to zero for others. In this case, we have $N_{T,S} \to \infty$, as suggested by (48). It means that the active segment at T_X should have a large number of elements so that all power is focused toward that L_X segment with a maximum R_X compensation gain. Another extreme case is for one-element L_X, where we note that (48) always suggests $N_{T,S} \to \infty$ to concentrate all transmitted power in that element. However, in all cases, we have the upper bound N_o so for $N_{T,S} > N_o$, we have $N_{T,S} = N_o$. For better performance, the value of N_o might be recalculated based on the portion of L_X that is selected by R_X beamforming only; however, this is considered for very large L_X sizes and close distances.

The second case is for $N_R = 1$, which is a worth-investigating practical case. With one antenna element at R_X, its compensation gain is equal at all L_X segments and we have

$$\left(N_{T,S} \right)_{\alpha'_{R;m}=1} = \sqrt{\frac{5S_L}{C'_1}}, \tag{51}$$

where $C'_1 = \sum_{m=1}^{S_L} \left(\gamma_{T,S} - \gamma_{T;m} \right)^2$. A closer look at (51) tells that $N_{T,S}$ is inversely proportional to the square root of the angular span of L_X segments. The larger the surface (or the deviation of its segments from the center if the coefficient S_L is included), the fewer the antenna elements that should be used. This might be explained by knowing that activating more elements with the beamforming design in (5) gets their signals added constructively at a narrower angular range around the beamforming angle (i.e., smaller beam size). At other directions, the signals with the same power add destructively. Therefore, it makes sense to enlarge the beam size as much as possible so that the signals add constructively in more directions, and this is what (51) suggests.

As seen in (48), the angular span of IRS determines the number of elements in the active segment. In this case we considered ULAs, but for uniform planer arrays (UPAs), the active segment is two-dimensional. Hence, the extension of the proposed scheme requires finding the number of elements in two dimensions by considering the span of IRS over the azimuth and elevation angles in the angular domain. Also, the extension to multiple IRSs responsible for first-order reflections is straightforward as each IRS has its beam at the transmitter. However, for second-order reflections by two

IRSs, the number of MPCs in the reflected signal increases and exceeds the number of phases that can be applied to them (i.e., the number of design degrees of freedom at the second beamforming tier). Therefore, focusing might not be an optimum solution between two IRSs and the two tiers need to be considered jointly, which is a case that requires further investigation.

In case of having a non-LoS link between T_X and L_X, searching for the best set of scatterers is first required. As mentioned earlier, L_X segments might experience different scatterers with T_X, further increasing design complexity. Furthermore, a non-LoS link between L_X and R_X requires an additional search for the best scatterers and increases the reflection order. In such cases, the minimum reflection order is two with additional overhead. On the other hand, first-order reflections are shown in this section to have less overhead and they have much higher power gain, concluding that LoS links with IRS are imperative. However, as L_X reflections are controlled and optimized, homogeneous higher-order reflections with no overhead are possible. In this case, the beamforming problem needs further investigation, as discussed earlier.

C. Numerical Results

As detailed previously, L_X was shown to be part of the channel as a scattering cluster with its own MPC as a specular component of the received signal by R_X. In this section, the performance of this cluster is investigated by means of simulations for the proposed beamforming scheme.

Cascaded beamforming was shown to have two cascaded parts: power collection and reflection. First, power collection is investigated, where L_X acts as a receiver with analog beamforming and it is desired to deliver it as much power as possible. Next, power reflection is addressed, where the achieved throughput by L_X specular component is shown for different scenarios. To focus on the performance of the controlled scattering cluster, we assume no scatterers in the environment except the controlled ones. Propagation parameters are $a_{\text{att}} = 2$ and $b_{\text{att}} = 2k$ for LoS links between system units [30]. The power radiation pattern of L_X elements is given as

$$B_e(\theta) = 2(2q+1)\cos^{2q}(\theta) \tag{52}$$

where θ is the element broadside angle and $q \approx 0.285$ is an introduced parameter to ensure power conservation [32]. Distances and sizes are given in terms of the wavelength, but the operating frequency is 28GHz. The transmitted power is set to 0dBm, and the noise floor is -90dBm. Antenna element spacing is selected for all system units to be $\lambda/2$. Simulations are conducted in the 2D space. Unless otherwise specified, T_X has 64 elements and it is laid on the x-axis with its center at $(0, 0)$. All system units are placed horizontally if orientation is not mentioned.

For one-element R_X, Fig. 7 and Fig. 8 show the path gain between T_X and L_X for different beamforming schemes under different L_X sizes and positioning. In Fig. 7, L_X is located at $(0, 933\lambda)$m, or $(0, 10)$m at the given operating frequency. For the plots in Fig. 8, on the other hand, L_X is located

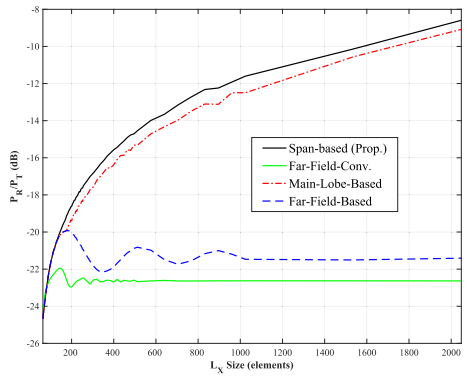

Fig. 7. Path gain for different beamforming schemes with L_X located perpendicular to T_X at $(0, 933\lambda)$.

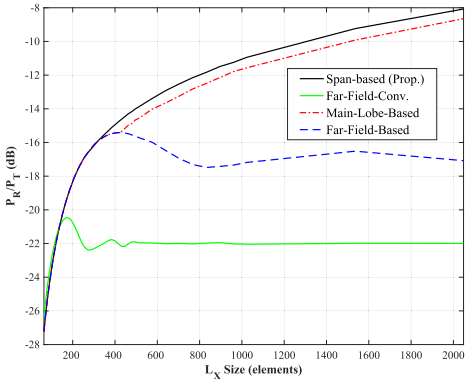

Fig. 8. Path gain for different beamforming schemes with L_X located at $(933\lambda, 933\lambda)$.

at $(933\lambda, 933\lambda)$m. Four cases are considered as follows. The one denoted by "Span-Based" is for the proposed scheme in the previous section, and "Far-Field-Conv" is given for the conventional beamforming that assumes far-field operation for all system units. The "Far-Field-Based" case is shown for a fixed active segment size depending on the distances with L_X elements regardless of its size. Finally, "Main-Lobe-Based" is given for the segment size selection that ensures covering L_X only by the main lobe, as long as it does not exceed the far-field-restricted segment size.

For IRS-size-independent schemes (i.e., far-field-based and far-field-conv methods), we note that the received signal power converges to a constant level. As L_X becomes larger, it will capture more power, regardless of how signals are precoded and combined. This continues until it becomes large enough to capture all main lobes of the kernels given in (21). For the main-Lobe-Based case, it is only one beam. The convergence power level depends on T_X and L_X angular spans as viewed by each other and the number of active elements at T_X. When T_X has a smaller angular span seen by L_X, L_X will be closer to operate in its far field. In the far field, conventional beamforming at T_X is optimum as the obtained power level is the best that can be captured.

For IRS-size-dependent active segmentation (i.e., span-based and main-lobe-based methods), we note that the power level keeps increasing. The reason is that these methods reduce the number of active elements as L_X gets larger, giving a chance to increase the main lobe size as discussed earlier. The main-lobe-based method shows how the proposed method

TABLE I

NUMBERS OF T_X ACTIVE ELEMENTS UNDER DIFFERENT BEAMFORMING SCHEMES FOR DIFFERENT L_X SIZES (IN ELEMENTS) AND POSITIONS

L_X**Location:**	$(0, 933\lambda)$			$(933\lambda, 933\lambda)$		
L_X**Size\Method**	Span-Based (Prop.)	Far-Field-Based	Main-Lobe-Based	Span-Based (Prop.)	Far-Field-Based	Main-Lobe-Based
2048	2	43	4	6	45	9
1024	5	43	8	12	48	20
512	9	43	15	25	50	41
256	18	43	29	51	51	51

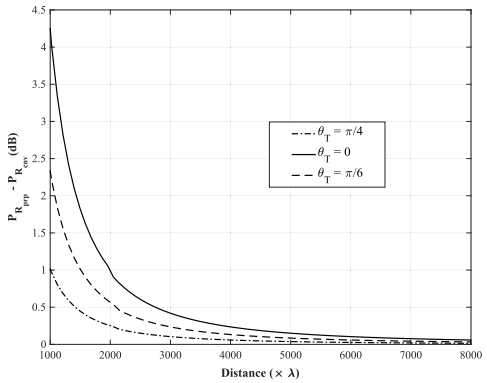

Fig. 9. Convergence of the proposed beamforming scheme to the conventional far-field scheme with distance.

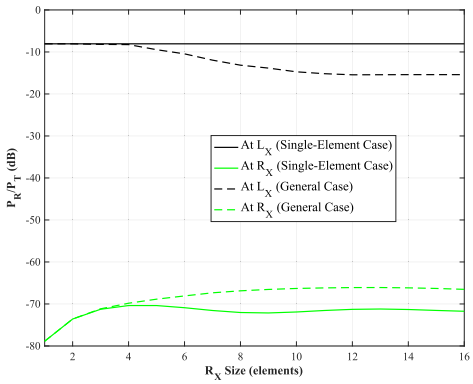

Fig. 10. Power levels at L_X and R_X with and without R_X beamforming effect.

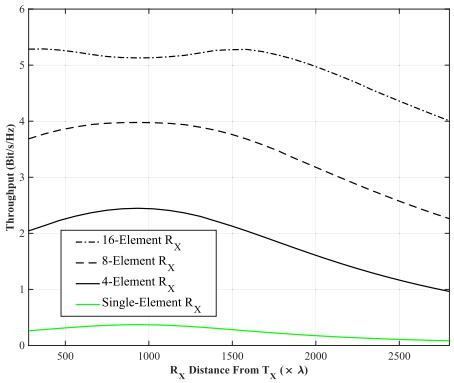

Fig. 11. Throughput achieved by the MPC reflected by L_X for different sizes of R_X at different locations.

performs just better than heuristically choosing to cover L_X surface by the main lobe of the active segment. It is only the case for one-element R_X; otherwise, the main-lobe-based method fails to account for R_X beamforming. Note here that using fewer elements serves better for large L_X sizes. Table I shows how the number of elements decreases for wider angular span by L_X. For example, based on the proposed method, 9 elements are recommended to deliver more power to an L_X with 512 elements located at $(0, 933\lambda)$m, though 43 elements are possible. Figures 7 and 8 show the difference between these two schemes, which is significant for larger L_X sizes. For smaller L_X spans, the two methods converge to the far-field-based method. At $(933\lambda, 933\lambda)$m, L_X has a smaller angular span and that explains why more elements are involved in both span-based and main-lobe-based methods.

The convergence of the proposed beamforming scheme to the conventional far-field scheme with distance is shown in Fig. 9. For demonstration purposes, T_X has only one element but R_X has 128 elements. The difference in power delivered by the two schemes decreases as R_X moves away from T_X since it becomes one segment and the proposed scheme decreases to the conventional one. However, for larger θ_T, which is the angular location of R_X with respect to the positive y-axis, the convergence is met faster. The reason is that R_X will have a smaller angular span seen by T_X, and as a result, its far-field boundary distance with T_X is smaller.

The number of active elements at T_X and L_X size were shown to be inversely proportional in the case of having one-element R_X. However, this is not the case when we have multiple elements at R_X as its beamforming has a selection effect over L_X segments. Figure 10 shows this effect. Both L_X and R_X are fixed in location at $(467\lambda, 467\lambda)$ and $(467\lambda, 0)$, respectively, and L_X size is 512λ. As the number of R_X elements increases, its compensation gain at those L_X segments far from its center is low. If the active segment at T_X is generated based on (51) as shown for the "Single-Element" case, the power received by R_X will be less compared with generation based on (48), which is the "General" case. The reason is that power is spread over the whole L_X surface in the signal-element case, though only a portion of the surface contributes to power reflection. On the other hand, when R_X beamforming is considered, despite having less power collected by L_X, more power is received at R_X. This is not to be confused with the desire to have the main lobe of the beam by T_X as large as possible.

The throughput achieved by the MPC of L_X at R_X with different sizes is shown in Fig. 11. L_X is located at $(933\lambda, 933\lambda)$ and R_X is moving from $(280\lambda, 0)$ to $(2800\lambda, 0)$. As might be expected, when getting closer to L_X, the throughput increases. This is clearly the case for small number of elements at R_X; however, as their number increases, due to receive beamforming, maximum throughput is achieved at other locations. At a perpendicular location, L_X will have the maximum angular span at R_X, and with more elements at L_X or R_X, there are more chances to get some L_X segments canceled by R_X beamforming. As R_X moves away, however, L_X occupies smaller angular span and more of its segments get accepted by beamforming at R_X.

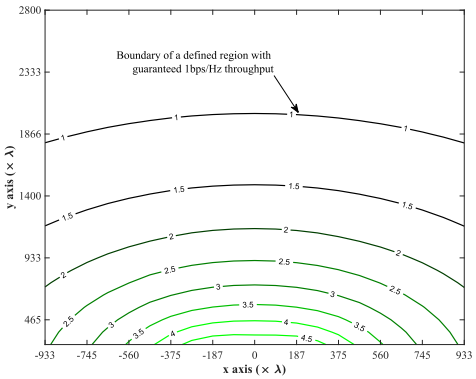

Fig. 12. Boundaries of defined regions with different levels of guaranteed throughputs.

Defined regions might be covered by one or more quasi-LoS links through IRSs. Figure 12 shows an example of the coverage provided by a single L_X within a given region. For this specific example, L_X size is 256λ and it is centered at $(0, 0)$. T_X is located at $(-933\lambda, 933\lambda)$. The throughput is calculated for a four-element R_X. A contour line represents the boundary of a region within which the capacity is guaranteed to be above its label number. We note that closer to L_X, the boundaries are not circular for the same reason explained earlier. However, far from L_X, this deviation is less, and the boundaries become more circular. Finally, the capacity drop with distance is not linear at all angles.

VI. Conclusion

In this work, IRS was investigated as part of the channel. Similar to any object in the environment, it acts as a scattering cluster but a controlled one. We have shown the way this control is possible and the nature of its reflected signal. By segmentation, each group of IRS elements is indeed a scatterer in the cluster.

A new model was proposed for the channel as a whole based on the classification of the MPC paths. By segmentation, we showed that the beam in the near field is a combination of kernels. Based on this model, a beamforming scheme was proposed to add those kernels constructively and maximize the received power.

The developed beam-space model shows how we really have a degree of control over the wireless channel, and how the channel can be converted from a problem to be part of the design. With its directed MPCs, the controlled cluster could open the door for new solutions in addressing both classical and emerging problems for future wireless network generations.

Appendix
Main-Lobe Approximation

Given that $e^{jx} = \sum_{s=0}^{\infty}(jx)^s/s!$, we have

$$f(\theta; N) = \sum_{l\in\mathcal{I}_N}\sum_{s=0}^{\infty}\frac{(j\theta l)^s}{s!} = \sum_{l\in\mathcal{I}_N}\sum_{k=0}^{\infty}\frac{(j\theta l)^{2k}}{(2k)!} \tag{53}$$

The second equality says that the imaginary part of the series cancels out due to the interval $\mathcal{I}_N$ symmetry around the zero. The main lobe of $f(\theta; N)$ carries most of its power. For our purpose in solving the beamforming problem, it is approximated by taking only $k \leq 1$ in (53), so we have the second-order polynomial

$$f_{\text{approx}}(\theta; N) = N - \theta^2 \sum_{l\in\mathcal{I}_N}\frac{l^2}{2} = N - \frac{N^3 - N}{24}\theta^2, \tag{54}$$

where in the second line we used the equality $\sum_{s=1}^{M} s^2 = M(M+1)(2M+1)/6$.

References

[1] C. Liaskos, S. Nie, A. Tsioliaridou, A. Pitsillides, S. Ioannidis, and I. Akyildiz, "A new wireless communication paradigm through software-controlled metasurfaces," *IEEE Commun. Mag.*, vol. 56, no. 9, pp. 162–169, Sep. 2018.

[2] E. Basar, M. Di Renzo, J. De Rosny, M. Debbah, M. Alouini, and R. Zhang, "Wireless communications through reconfigurable intelligent surfaces," *IEEE Access*, vol. 7, pp. 116753–116773, 2019.

[3] M. Di Renzo *et al.*, "Smart radio environments empowered by reconfigurable intelligent surfaces: How it works, state of research, and the road ahead," *IEEE J. Sel. Areas Commun.*, vol. 38, no. 11, pp. 2450–2525, Nov. 2020.

[4] S. Zhang and R. Zhang, "Capacity characterization for intelligent reflecting surface aided MIMO communication," *IEEE J. Sel. Areas Commun.*, vol. 38, no. 8, pp. 1823–1838, Aug. 2020.

[5] J. Qiao and M.-S. Alouini, "Secure transmission for intelligent reflecting surface-assisted mmWave and terahertz systems," *IEEE Wireless Commun. Lett.*, vol. 9, no. 10, pp. 1743–1747, Oct. 2020.

[6] H. Shen, W. Xu, S. Gong, Z. He, and C. Zhao, "Secrecy rate maximization for intelligent reflecting surface assisted multi-antenna communications," *IEEE Commun. Lett.*, vol. 23, no. 9, pp. 1488–1492, Sep. 2019.

[7] M. Cui, G. Zhang, and R. Zhang, "Secure wireless communication via intelligent reflecting surface," *IEEE Wireless Commun. Lett.*, vol. 8, no. 5, pp. 1410–1414, Oct. 2019.

[8] Q. Wu and R. Zhang, "Intelligent reflecting surface enhanced wireless network via joint active and passive beamforming," *IEEE Trans. Wireless Commun.*, vol. 18, no. 11, pp. 5394–5409, Nov. 2019.

[9] C. Huang, A. Zappone, G. C. Alexandropoulos, M. Debbah, and C. Yuen, "Reconfigurable intelligent surfaces for energy efficiency in wireless communication," *IEEE Trans. Wireless Commun.*, vol. 18, no. 8, pp. 4157–4170, Aug. 2019.

[10] P. Wang, J. Fang, X. Yuan, Z. Chen, and H. Li, "Intelligent reflecting surface-assisted millimeter wave communications: Joint active and passive precoding design," *IEEE Trans. Veh. Technol.*, vol. 69, no. 12, pp. 14960–14973, Dec. 2020.

[11] Q.-U.-A. Nadeem, A. Kammoun, A. Chaaban, M. Debbah, and M.-S. Alouini, "Asymptotic max-min SINR analysis of reconfigurable intelligent surface assisted MISO systems," *IEEE Trans. Wireless Commun.*, vol. 19, no. 12, pp. 7748–7764, Apr. 2020.

[12] Z. Ding and H. V. Poor, "A simple design of IRS-NOMA transmission," *IEEE Commun. Lett.*, vol. 24, no. 5, pp. 1119–1123, May 2020.

[13] T. Hou, Y. Liu, Z. Song, X. Sun, Y. Chen, and L. Hanzo, "Reconfigurable intelligent surface aided NOMA networks," *IEEE J. Sel. Areas Commun.*, vol. 38, no. 11, pp. 2575–2588, Nov. 2020.

[14] A. Almohamad *et al.*, "Smart and secure wireless communications via reflecting intelligent surfaces: A short survey," *IEEE Open J. Commun. SoC.*, vol. 1, pp. 1442–1456, 2020.

[15] S. Gong *et al.*, "Toward smart wireless communications via intelligent reflecting surfaces: A contemporary survey," *IEEE Commun. Surveys Tuts.*, vol. 22, no. 4, pp. 2283–2314, 4th Quart., 2020.

[16] C. You, B. Zheng, and R. Zhang, "Channel estimation and passive beamforming for intelligent reflecting surface: Discrete phase shift and progressive refinement," *IEEE J. Sel. Areas Commun.*, vol. 38, no. 11, pp. 2604–2620, Nov. 2020.

[17] S. Eddine Zegrar, L. Afeef, and H. Arslan, "A general framework for RIS-aided mmWave communication networks: Channel estimation and mobile user tracking," 2020, *arXiv:2009.01180*.

[18] S. Eddine Zegrar, L. Afeef, and H. Arslan, "Reconfigurable intelligent surface (RIS): Eigenvalue decomposition-based separate channel estimation," 2020, *arXiv:2010.05623*.
[19] S. Liu, Z. Gao, J. Zhang, M. D. Renzo, and M.-S. Alouini, "Deep denoising neural network assisted compressive channel estimation for mmWave intelligent reflecting surfaces," *IEEE Trans. Veh. Technol.*, vol. 69, no. 8, pp. 9223–9228, Aug. 2020.
[20] Z.-Q. He and X. Yuan, "Cascaded channel estimation for large intelligent metasurface assisted massive MIMO," *IEEE Wireless Commun. Lett.*, vol. 9, no. 2, pp. 210–214, Feb. 2020.
[21] C.-X. Wang, J. Bian, J. Sun, W. Zhang, and M. Zhang, "A survey of 5G channel measurements and models," *IEEE Commun. Surveys Tuts.*, vol. 20, no. 4, pp. 3142–3168, 4th Quart., 2018.
[22] W. Roh *et al.*, "Millimeter-wave beamforming as an enabling technology for 5G cellular communications: Theoretical feasibility and prototype results," *IEEE Commun. Mag.*, vol. 52, no. 2, pp. 106–113, Feb. 2014.
[23] T. S. Rappaport, G. R. Maccartney, M. K. Samimi, and S. Sun, "Wideband millimeter-wave propagation measurements and channel models for future wireless communication system design," *IEEE Trans. Commun.*, vol. 63, no. 9, pp. 3029–3056, Sep. 2015.
[24] M. Peter, K. Haneda, S. Nguyen, A. Karttunen, and J. Järveläinen, "Measurement results and final mmMAGIC channel models," *Deliverable*, vol. 2, p. 12, May 2017.
[25] A. Maltsev, R. Maslennikov, A. Sevastyanov, A. Khoryaev, and A. Lomayev, "Experimental investigations of 60 GHz WLAN systems in office environment," *IEEE J. Sel. Areas Commun.*, vol. 27, no. 8, pp. 1488–1499, Oct. 2009.
[26] J. Zhang *et al.*, "Prospective multiple antenna technologies for beyond 5G," *IEEE J. Sel. Areas Commun.*, vol. 38, no. 8, pp. 1637–1660, Aug. 2020.
[27] A. M. Sayeed, "Deconstructing multiantenna fading channels," *IEEE Trans. Signal Process.*, vol. 50, no. 10, pp. 2563–2579, Oct. 2002.
[28] D. Tse and P. Viswanath, *Fundamentals Wireless Communication*, (Wiley Series in Telecommunications). Cambridge, U.K.: Cambridge Univ. Press, 2005.
[29] I. A. Hemadeh, K. Satyanarayana, M. El-Hajjar, and L. Hanzo, "Millimeter-wave communications: Physical channel models, design considerations, antenna constructions, and link-budget," *IEEE Commun. Surveys Tuts.*, vol. 20, no. 2, pp. 870–913, 2nd Quart., 2018.
[30] E. Basar, I. Yildirim, and F. Kilinc, "Indoor and outdoor physical channel modeling and efficient positioning for reconfigurable intelligent surfaces in mmWave bands," *IEEE Trans. Commun.*, early access, Sep. 20, 2021, doi: 10.1109/TCOMM.2021.3113954.
[31] W. Wang and W. Zhang, "Joint beam training and positioning for intelligent reflecting surfaces assisted millimeter wave communications," *IEEE Trans. Wireless Commun.*, vol. 20, no. 10, pp. 6282–6297, Oct. 2021.
[32] S. W. Ellingson, "Path loss in reconfigurable intelligent surface-enabled channels," 2019, *arXiv:1912.06759*.
[33] W. Tang *et al.*, "Wireless communications with reconfigurable intelligent surface: Path loss modeling and experimental measurement," *IEEE Trans. Wireless Commun.*, vol. 20, no. 1, pp. 421–439, Jan. 2021.
[34] O. Özdogan, E. Björnson, and E. G. Larsson, "Intelligent reflecting surfaces: Physics, propagation, and pathloss modeling," *IEEE Wireless Commun. Lett.*, vol. 9, no. 5, pp. 581–585, May 2020.
[35] G. Gradoni and M. Di Renzo, "End-to-end mutual coupling aware communication model for reconfigurable intelligent surfaces: An electromagnetic-compliant approach based on mutual impedances," *IEEE Wireless Commun. Lett.*, vol. 10, no. 5, pp. 938–942, May 2021.
[36] F. Yang and Y. Rahmat-Samii, *Surface Electromagnetics: With Applications in Antenna, Microwave, and Optical Engineering*. Cambridge, U.K.: Cambridge Univ. Press, 2019.
[37] B. Friedlander, "Localization of signals in the near-field of an antenna array," *IEEE Trans. Signal Process.*, vol. 67, no. 15, pp. 3885–3893, Aug. 2019.
[38] K. T. Selvan and R. Janaswamy, "Fraunhofer and Fresnel distances: Unified derivation for aperture antennas," *IEEE Antennas Propag. Mag.*, vol. 59, no. 4, pp. 12–15, Aug. 2017.
[39] O. El Ayach, S. Rajagopal, S. Abu-Surra, Z. Pi, and R. W. Heath, Jr., "Spatially sparse precoding in millimeter wave MIMO systems," *IEEE Trans. Wireless Commun.*, vol. 13, no. 3, pp. 1499–1513, Mar. 2014.
[40] J. Brady, N. Behdad, and A. M. Sayeed, "Beamspace MIMO for millimeter-wave communications: System architecture, modeling, analysis, and measurements," *IEEE Trans. Antennas Propag.*, vol. 61, no. 7, pp. 3814–3827, Jul. 2013.
[41] A. Alkhateeb and R. W. Heath, Jr., "Frequency selective hybrid precoding for limited feedback millimeter wave systems," *IEEE Trans. Commun.*, vol. 64, no. 5, pp. 1801–1818, May 2016.
[42] A. Maltsev, *Channel Models for IEEE 802.11ay*, document 802.11-15/1150r9, 2017.
[43] A. Meijerink and A. F. Molisch, "On the physical interpretation of the Saleh-Valenzuela model and the definition of its power delay profiles," *IEEE Trans. Antennas Propag.*, vol. 62, no. 9, pp. 4780–4793, Sep. 2014.
[44] I. S. Gradshteyn and I. M. Ryzhik, *Table of Integrals, Series, and Products*. New York, NY, USA: Academic, 2014.
[45] X. Gao, F. Tufvesson, and O. Edfors, "Massive MIMO channels—Measurements and models," in *Proc. Asilomar Conf. Signals, Syst. Comput.*, Nov. 2013, pp. 280–284.
[46] C. F. López and C.-X. Wang, "Novel 3-D non-stationary wideband models for massive MIMO channels," *IEEE Trans. Wireless Commun.*, vol. 17, no. 5, pp. 2893–2905, May 2018.

Musab Alayasra (Student Member, IEEE) received the B.E. degree in electrical engineering from the Jordan University of Science and Technology, Irbid, Jordan, in 2015. He is currently pursuing the Ph.D. degree with the Communications, Signal Processing, and Networking Center (CoSiNC), Istanbul Medipol University, Turkey. He is also a Research Assistant at CoSiNC. His current research interest includes intelligent reflecting surfaces for wireless communications.

Hüseyin Arslan (Fellow, IEEE) received the B.S. degree from Middle East Technical University (METU), Ankara, Turkey, in 1992, and the M.S. and Ph.D. degrees from Southern Methodist University (SMU), Dallas, TX, USA, in 1994 and 1998, respectively.

From January 1998 to August 2002, he was with the Research Group of Ericsson, where he was involved with several projects related to 2G and 3G wireless communication systems. Since August 2002, he has been with the Electrical Engineering Department, University of South Florida, where he is currently a Professor. He joined Istanbul Medipol University to found the Engineering College, in December 2013, where he worked as the Dean of the School of Engineering and Natural Sciences. In addition, he worked as a part-time Consultant for various companies and institutions, including Anritsu Company and The Scientific and Technological Research Council of Turkey. He conducts research in wireless systems, with emphasis on the physical and medium access layers of communications. He has been collaborating extensively with key national and international industrial partners and his research has generated significant interest in companies, such as InterDigital, Anritsu, NTT DoCoMo, Raytheon, Honeywell, Keysight Technologies. Collaborations and feedback from industry partners has significantly influenced his research. In addition to his research activities, he has also contributed to wireless communication education. He has integrated the outcomes of his research into education which lead him to develop a number of courses at the University of South Florida. He has developed a unique "Wireless Systems Laboratory" course (funded by the National Science Foundation and Keysight Technologies) where he was able to teach not only the theory but also the practical aspects of wireless communication system with the most contemporary test and measurement equipment. His current research interests include 5G and beyond radio access technologies, physical layer security, interference management (avoidance, awareness, and cancellation), cognitive radio, multi-carrier wireless technologies (beyond OFDM), dynamic spectrum access, co-existence issues, non-terrestrial communications (high altitude platforms), and joint radar (sensing) and communication designs.

Dr. Arslan is also a member of the Editorial Board of the IEEE COMMUNICATIONS SURVEYS AND TUTORIALS and the *Sensors* journal. He has also served as a member of the editorial board for the IEEE TRANSACTIONS ON COMMUNICATIONS, the IEEE TRANSACTIONS ON COGNITIVE COMMUNICATIONS AND NETWORKING (TCCN), and several other scholarly journals by Elsevier, Hindawi, and Wiley Publishing. He has served as the general chair, the technical program committee chair, the session and symposium organizer, the workshop chair, and a technical program committee member in several IEEE conferences.